ADVANCED FUNCTIONAL MATERIALS
www.afm-journal.de

Manifestation of Strongly Correlated Electrons in a 2D Kagome Metal–Organic Framework

*Dhaneesh Kumar, Jack Hellerstedt, Bernard Field, Benjamin Lowe, Yuefeng Yin, Nikhil V. Medhekar, and Agustin Schiffrin**

2D and layered electronic materials characterized by a kagome lattice, whose valence band structure includes two Dirac bands and one flat band, can host a wide range of tunable topological and strongly correlated electronic phases. While strong electron correlations have been observed in inorganic kagome crystals, they remain elusive in organic systems, which benefit from versatile synthesis protocols via molecular self-assembly and metal-ligand coordination. Here, direct experimental evidence of local magnetic moments resulting from strong electron–electron Coulomb interactions in a 2D metal–organic framework (MOF) is reported. The latter consists of di-cyano-anthracene (DCA) molecules arranged in a kagome structure via coordination with copper (Cu) atoms on a silver surface [Ag(111)]. Temperature-dependent scanning tunneling spectroscopy reveals magnetic moments spatially confined to DCA and Cu sites of the MOF, and Kondo screened by the Ag(111) conduction electrons. By density functional theory and mean-field Hubbard modeling, it is shown that these magnetic moments are the direct consequence of strong Coulomb interactions between electrons within the kagome MOF. The findings pave the way for nanoelectronics and spintronics technologies based on controllable correlated electron phases in 2D organic materials.

1. Introduction

2D materials with a kagome crystal structure—where atoms or molecules are arranged in corner-sharing equilateral triangles (see **Figure 1**)—can host electronic wavefunctions that interfere destructively, resulting in highly localized electronic states.[1–3] These states, when filled gradually, give rise to increasing Coulomb electron-electron interactions, with characteristic energies that can be significantly larger than the valence bandwidth.[4] These strong Coulomb interactions, tunable via the valence band (VB) electronic population, can lead to a vast range of quantum correlated electron phenomena, including magnetic ordering of unpaired electron spins (i.e., magnetic moments, resulting in, for example, ferro-[5] or antiferromagnetic phases[6]), quantum spin liquids,[7] metal-to-insulator Mott transitions,[8] and non-trivial topology.[9–11] This tunability between versatile and fundamentally diverse quantum phenomena offers promise for electronics and spintronics applications based on controllable electron correlations in 2D materials.

When interfacing with a metal (e.g., substrate, electrode), local magnetic moments (that is, spatially confined at the nanoscale to specific locations) that result from electron-electron Coulomb interactions in a material (e.g., with 2D kagome structure) can become screened by the metal conduction electrons, giving rise to the many-body Kondo effect.[6,12,13] This effect results in a resonance in the system's density of electronic states (DOS) at the Fermi level, which vanishes above a characteristic Kondo temperature, T_K. That is, the measurement of a Kondo resonance in the DOS of a material interfacing with a metal can reveal the presence of local magnetic moments, and hence serve as a direct experimental probe for strong electron-electron interactions within the system.

Recently, correlated electron phenomena and flat electronic bands have been observed in inorganic 2D kagome materials.[6,14,15] Metal–organic frameworks[4,9] (MOFs) and covalent organic frameworks[16] (COFs) with similar structure and electronic properties have been predicted, with the additional promise of tunable electron-electron interactions and topology via versatile, atomically precise synthesis approaches based on metal–organic coordination[17] and organic covalent bonding.[18] While 2D kagome MOFs and COFs have been synthesized, neither flat bands nor correlated electron phenomena have yet been observed in these systems.[19–23]

Here, we report direct experimental evidence of magnetic moments locally confined to specific sites of a 2D MOF on a weakly interacting[24] Ag(111) surface. These local magnetic moments are revealed via temperature-dependent scanning tunneling spectroscopy (STS) measurements of Kondo

D. Kumar, J. Hellerstedt, B. Field, B. Lowe, Y. Yin, A. Schiffrin
School of Physics & Astronomy
Monash University
Clayton, Victoria 3800, Australia
E-mail: agustin.schiffrin@monash.edu

D. Kumar, J. Hellerstedt, B. Field, B. Lowe, Y. Yin, N. V. Medhekar, A. Schiffrin
ARC Centre of Excellence in Future Low-Energy Electronics Technologies
Monash University
Clayton, Victoria 3800, Australia

Y. Yin, N. V. Medhekar
Department of Materials Science and Engineering
Monash University
Clayton, Victoria 3800, Australia

The ORCID identification number(s) for the author(s) of this article can be found under https://doi.org/10.1002/adfm.202106474.

DOI: 10.1002/adfm.202106474

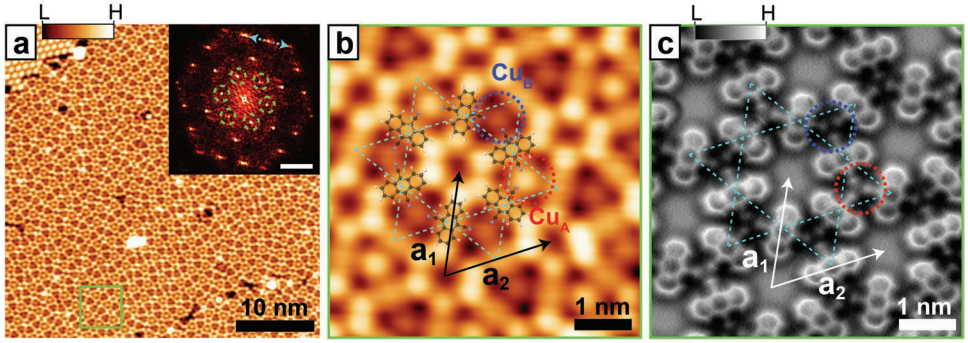

Figure 1. Atomically thin kagome MOF on a noble metal surface. a) STM image of the DCA_3Cu_2 kagome structure on Ag(111) ($V_b = -20$ mV, $I_t = 50$ pA). Inset: Fourier transform (FT; $|\mathbf{k}| = 1/\text{wavelength}$; scale bar: 1 nm^{-1}) of STM image. Green dashed circles indicate 1st harmonic peaks corresponding to the MOF hexagonal lattice. Anisotropic stretching of peaks (dashed cyan arrow) and diffuse background (around $\mathbf{k} = 0$) of FT are due to lack of perfect long-range order. b,c) STM (b; $V_b = -20$ mV, $I_t = 50$ pA) and tip-functionalized (CO) nc-AFM (c; tip retracted 0.3 Å with respect to STM set point, $V_b = 3$ mV, $I_t = 150$ pA, adjusted on top of DCA molecule center) images of region indicated by green box in (a), with DCA chemical structure superimposed (black: carbon; blue: nitrogen; white: hydrogen). Vectors $\mathbf{a}_1$, $\mathbf{a}_2$ define a primitive unit cell ($\|\mathbf{a}_1\| = \|\mathbf{a}_2\| = 2.045$ nm; $\measuredangle(\mathbf{a}_1,\mathbf{a}_2) = 60°$). Dashed cyan lines show the molecular kagome arrangement. Cu atoms can have two different STM and nc-AFM apparent heights differing by ≈19 pm ("Cu_A" and "Cu_B", dashed circles; Figure S4, Supporting Information).

screening by the Ag(111) conduction electrons. The 2D MOF consists of di-cyano-anthracene (DCA) molecules arranged in a kagome geometry via coordination with copper (Cu) atoms. We show, by density functional theory (DFT) (including corrections for on-site electron-electron interactions; DFT+U) and a mean-field Hubbard (MFH) model, that the magnetic moments result directly from strong correlations between electrons within the kagome MOF.

2. Results and Discussion

We synthesized the 2D kagome MOF by depositing DCA molecules and Cu onto Ag(111) in ultrahigh vacuum (UHV; see Experimental Section). Each DCA cyano group coordinates with a Cu atom, forming a DCA (Cu) kagome (honeycomb, respectively) arrangement with a primitive unit cell composed of 3 DCA molecules and 2 Cu adatoms[20,25,26] (see scanning tunneling (STM) and non-contact atomic force (nc-AFM) microscopy images in Figure 1). We observe two types of Cu atoms (labeled Cu_A and Cu_B in Figure 1) with slightly different adsorption heights (see Figure S4, Supporting Information). The 2D MOF structure is not perfectly crystalline (Figure 1a) due to incommensurability with the underlying substrate (Figures S1 and S2, Supporting Information).

For insights into the local density of electronic states (LDOS) of the MOF on Ag(111), we performed differential conductance (dI/dV) STS at 4.4 K. **Figure 2**a shows spectra taken at the DCA center, DCA anthracene extremity, Cu atom, and MOF pore center. The latter exhibits a broad resonance between 150–500 mV attributed to the confinement of the Ag(111) Shockley surface state (SSS) by the MOF, similar to the case of DCA_3Cu_2 on Cu(111)[25] (Section S2, Supporting Information). Due to this confinement, the Ag(111) SSS onset energy is shifted above the Fermi level: the SSS is depopulated[24,27] and hence does not affect the system's electronic properties reported below.

In the following, we focus on dI/dV features near the Fermi level (Figure 2b). Spectra taken at the DCA anthracene extremities and Cu atoms show zero-bias peaks (ZBPs). Spectra at Cu_B sites are qualitatively identical to those at Cu_A sites but with reduced intensity, henceforth, we focus just on Cu_A. At the molecule center, we observe a pair of prominent step-like features at ≈±43 mV, and satellite peaks at ≈±17, ≈±43, and ≈±75 mV, symmetric in energy with respect to the Fermi level (with more subtle peaks at ≈±56 and ≈±86 mV; Figure S11, Supporting Information). These peaks are also observed at the anthracene extremity and Cu locations (grey dashed lines, Figure 2b). Spatial mapping of these dI/dV features is shown in Figure 2c (zero bias) and 2d (–100 mV, below the bias onset of the step-like feature in Figure 2b; see Figure S7, Supporting Information, for dI/dV maps related to satellite peaks).

To understand the nature of the ZBP and the energy-symmetric off-Fermi features, we acquired dI/dV spectra at the Cu, anthracene extremity, and DCA center sites, for temperatures, T, between 4.4 and 145 K (**Figure 3**a–c). We observed that the ZBP and off-Fermi features diminish in magnitude and broaden with increasing T. We fit each spectrum with the function:[28]

$$\int_{-\infty}^{\infty} \rho_{\text{fit}}(E,T)\frac{\mathrm{d}}{\mathrm{d}V} f_{\text{FD}}(E-eV,T)\,\mathrm{d}E \tag{1}$$

where f_{FD} is the Fermi–Dirac distribution (accounting for thermal broadening), V is the bias voltage and e is the absolute value of the electron charge. For the Cu and anthracene extremity sites, ρ_{fit} consists of the sum of 2 pairs of Lorentzians (accounting for the energy-symmetric off-Fermi peaks) and a Fano line shape (accounting for the ZBP):

$$f_{\text{Fano}}(V) \propto \frac{(\varepsilon(V)+q)^2}{\varepsilon(V)^2+1}, \varepsilon(V) = \frac{eV-E_0}{\Gamma_{\text{Fano}}} \tag{2}$$

where q is the Fano line shape parameter, E_0 is the ZBP energy position, and Γ_{Fano} is the Fano line width (Section S6, Supporting Information, for fitting details). For the anthracene extremity ZBP, $q = \infty$, that is, the corresponding Fano line is a Lorentzian (Figure 3b). For the DCA center (Figure 3c), ρ_{fit} consists of

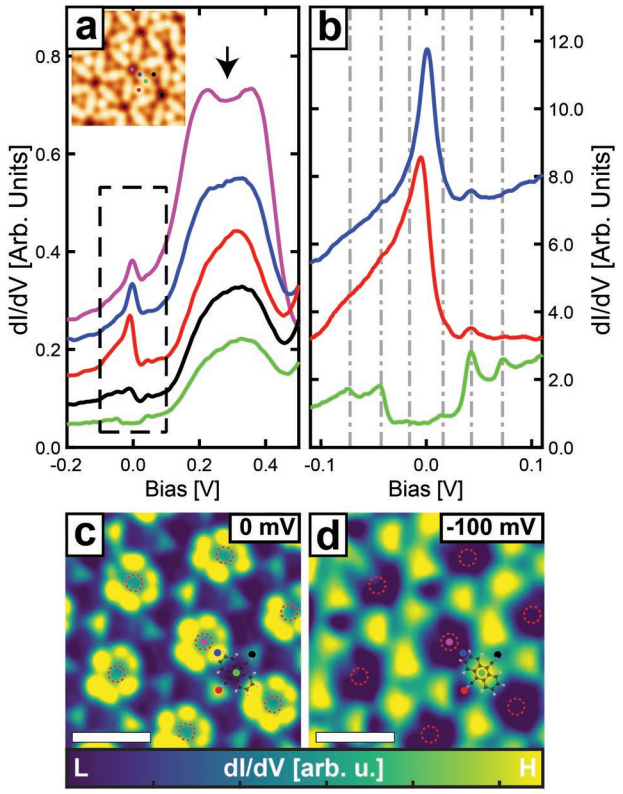

Figure 2. Electronic properties of DCA_3Cu_2 kagome MOF on Ag(111): local density of states resonances near the Fermi level. a) d*I*/d*V* STS spectra (set point $V_b = -250$ mV, $I_t = 0.5$ nA; offset for clarity) at high symmetry points of kagome MOF (indicated in inset STM image; $V_b = -200$ mV, $I_t = 0.5$ nA). Broad resonance between 0.15–0.5 V (black arrow) attributed to Ag(111) Shockley surface state confined within kagome pores (see Section S2, Supporting Information). b) Near-Fermi d*I*/d*V* STS spectra (dashed rectangle in (a)) at DCA anthracene extremity (blue) and MOF Cu (Cu_A) atom (red), showing sharp zero-bias resonances, and at DCA center (green), showing a prominent step at ≈±43 mV and peaks at ≈±17, ±43, and ±75 mV (indicated by vertical grey dashed lines, and related to inelastic tunneling due to DCA vibrational modes; see Section S6, Supporting Information). c,d) d*I*/d*V* maps at 0 and −100 mV (following STM topography with tip retracted 120 and 30 pm, respectively, with respect to set point $V_b = -200$ mV, $I_t = 0.5$ nA; see Experimental Section), showing spatial distributions of ZBP (with significant d*I*/d*V* intensity at anthracene extremities and Cu atoms) and of energy-symmetric off-Fermi satellite features (with significant d*I*/d*V* intensity at anthracene centers), respectively. Red dashed circles: pores of kagome MOF. Scale bars: 1.5 nm.

the sum of 5 pairs of Lorentzians (energy-symmetric off-Fermi peaks) and a pair of step functions (features at ±43 mV).

The Fano line width, Γ_{Fano}, for the Cu and anthracene extremity ZBPs increases as a function of T (Figure 3d), beyond trivial thermal broadening; if the ZBP broadening were exclusively due to broadening of the Fermi–Dirac distribution, $\Gamma_{Fano}(T)$ would be constant, and the ZBP could be explained by an intrinsic MOF electronic state. We fit $\Gamma_{Fano}(T)$ with the expression:

$$\Gamma_{Fano}(T) = \sqrt{2(k_B T_K)^2 + (\pi k_B T)^2} \quad (3)$$

where k_B is the Boltzmann constant and T_K is a fitting parameter that we discuss below (Figure 3d). We obtained $T_K = 125 \pm 7$ K

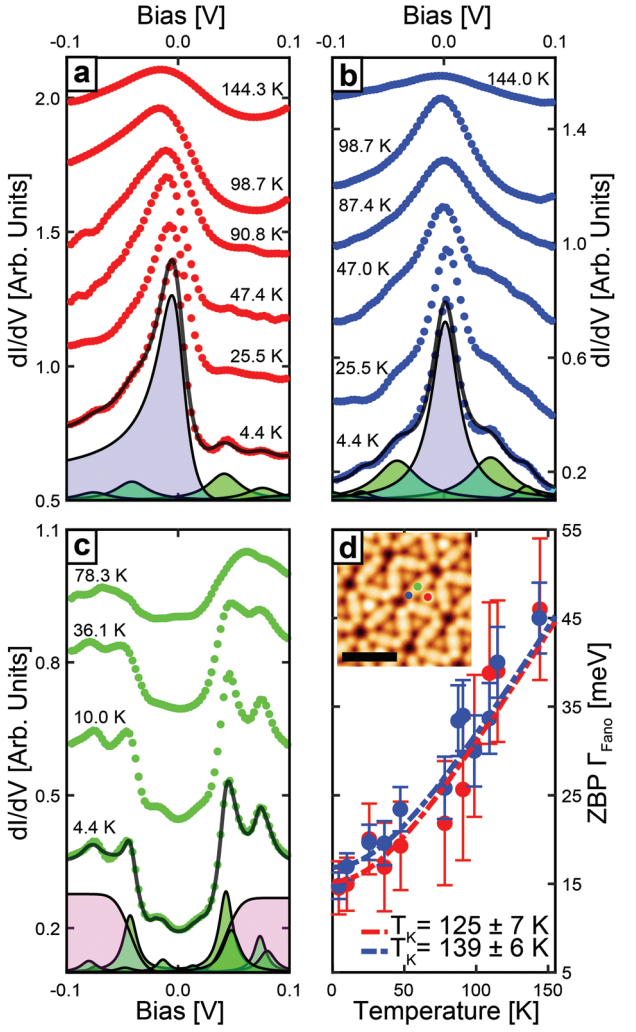

Figure 3. Temperature-dependent near-Fermi d*I*/d*V* spectra: evidence of the Kondo effect. a–c) Background-subtracted d*I*/d*V* spectra at Cu (red data points; here, Cu_A), DCA anthracene extremity (blue) and DCA center (green), taken at various temperatures, *T*. Black curves: total fits of $T = 4.4$ K data, consisting of a Fano line shape for the ZBP (blue filled curves), pairs of Lorentzians for the energy-symmetric off-Fermi peaks (green filled) and a pair of error functions for the energy-symmetric step functions (magenta filled). d) Width, Γ_{Fano}, of ZBP fit Fano line shape in (a,b), for Cu (red) and DCA anthracene extremity (blue), as a function of *T*. Effect of thermal broadening is accounted for (see Section S6, Supporting Information). Dashed curves: fitting of $\Gamma_{Fano}(T)$ with Equation (3) in text, resulting in $T_K = 125 \pm 7$ and 139 ± 6 K for Cu_A and anthracene extremity, respectively. Inset: STM image of DCA_3Cu_2 MOF ($V_b = -250$ mV, $I_t = 1.5$ nA), with locations at which d*I*/d*V* spectra in (a–c) are obtained; scale bar: 2 nm.

and $T_K = 139 \pm 6$ K for Cu_A and the DCA anthracene extremity sites, respectively (Figure S9, Supporting Information, for Cu_B site $\Gamma_{Fano}(T)$).

Equation (3) describes the temperature dependence of Γ_{Fano} for the Fermi level resonance observed in the LDOS in the case of the Kondo effect.[6,12,13] That is, when a magnetic moment spatially confined to a specific location (i.e., *local*) is screened by the spins of surrounding, delocalized conduction electrons, with T_K reflecting the coupling strength between the local moment and conduction electrons' spins. Given the agreement between our

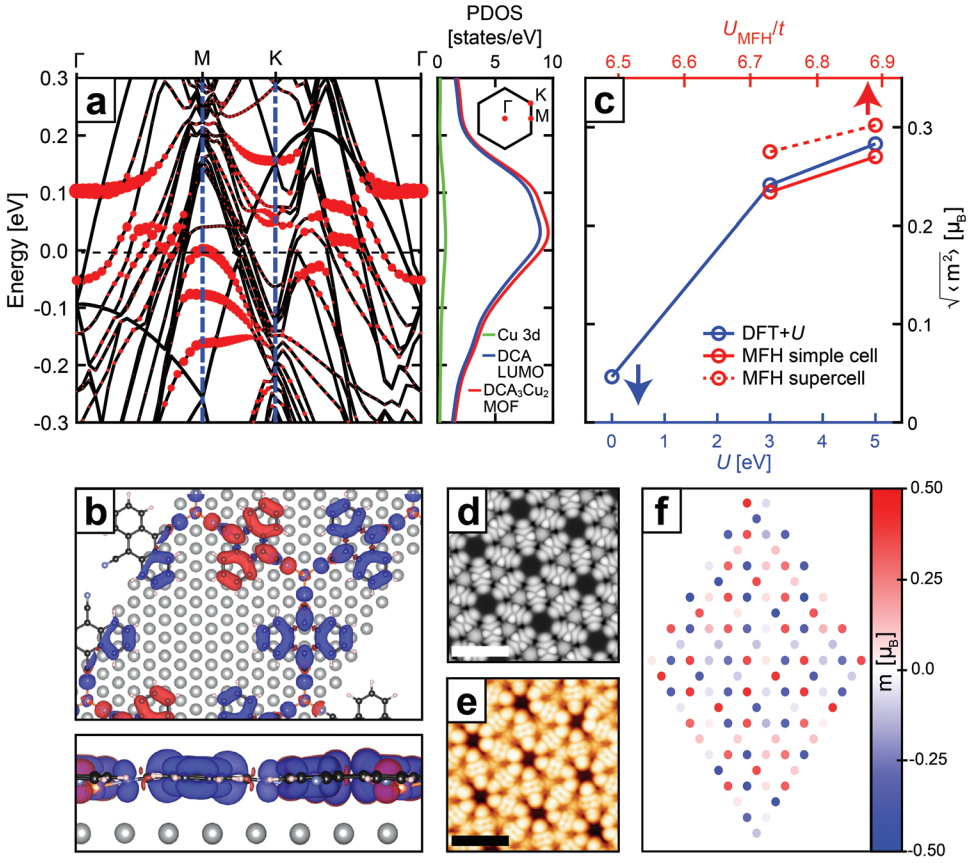

Figure 4. Theoretical calculations: emergence of local magnetic moments due to strong electron–electron Coulomb interactions. a) Band structure (along reciprocal space high-symmetry points) and projected density of states (PDOS) of DCA_3Cu_2 MOF on Ag(111) calculated by DFT ($U = 0$). Red circles and curve correspond to projections onto DCA_3Cu_2 MOF orbitals. Kagome bands have predominantly DCA LUMO character, with slight Cu 3*d* contribution due to partial hybridization between LUMO and Cu 3*d* orbitals. b) Ground state magnetic moment density isosurface (2×10^{-4} μ_B Å^{-3}; top and side views) of DCA_3Cu_2/Ag(111), calculated via DFT+*U* ($U = 3$ eV), following the spatial distribution of the near-Fermi DCA_3Cu_2 MOF orbitals (with dominant contributions from DCA LUMOs, the latter partially populated by Cu 4*s* electrons upon Cu-DCA coordination). Note magnetic moment orientations (red: up; blue: down) indicating frustrated antiferromagnetic coupling. c) Average magnetic moment per DCA molecule, calculated for DCA_3Cu_2/Ag(111) via DFT+*U* as a function of *U* (blue; single unit cell; see Experimental Section), and via MFH model (solid red curve: primitive unit cell consisting of 3 kagome sites; dashed red curve: large supercell as in (f)) for freestanding DCA_3Cu_2 with $U_{MFH} = 6.73t$ and $6.89t$ (electron filling of 0.3, tuned to match MOF-to-surface electron transfer of $\approx 0.20e^-$ per primitive unit cell given by DFT+*U* for DCA_3Cu_2/Ag(111) with $U = 3$ and 5 eV; see Experimental Section and Supporting Information). The larger average local magnetic moment for the supercell results from the greater magnetic configurational freedom (Section S9, Supporting Information). d) Simulated STM image of DCA_3Cu_2/Ag(111) derived from DFT+*U* calculations ($U = 3$ eV; $V_b = -100$ mV; see Experimental Section). e) Experimental STM image of DCA_3Cu_2/Ag(111) (tip functionalized with a CO molecule, $V_b = -20$ mV, $I_t = 25$ pA). Scale bars: 2 nm. Experimental and simulated STM images show good agreement, in particular, regarding orbital nodal planes perpendicular to anthracene axis, lobes at anthracene extremities, and threefold rotationally symmetric imaging of Cu sites; slight quantitative discrepancies can be due to CO-tip not taken into account in simulation. f) Ground state magnetic moments for DCA kagome sites in freestanding DCA_3Cu_2 MOF (supercell), calculated by MFH model ($U_{MFH} = 6.73t$, electron filling: 0.30).

temperature-dependent dI/dV data in Figure 3 and Equation (3), we attribute the observed ZBP to Kondo screening of unpaired local magnetic moments within the MOF by Ag(111) conduction electrons. Our values for $T_K > 120$ K, are similar to those observed for unpaired electron spins in other π-conjugated molecule-on-metal systems.[29] The ZBP was neither observed for DCA on Ag(111) (without Cu)[24] nor in other non-kagome 2D MOFs based on Cu-cyano coordination on Ag(111);[30] therefore, it is a property specific to the DCA_3Cu_2 kagome MOF.

We attribute the energy-symmetric, off-Fermi step features and peaks in the dI/dV spectra (within ±100 meV of the Fermi level; Figure 3a–c) to inelastic excitations of MOF vibrational modes.[31] This is consistent with DFT (Experimental Section) calculations (see Section S6, Supporting Information). In particular, the off-Fermi peaks are due to the vibrationally-assisted Kondo effect,[32] resulting from coupling between such MOF vibrational modes and magnetic moments.

The observation of the Kondo effect in our DCA_3Cu_2/Ag(111) system provides compelling evidence for the presence of magnetic moments within the MOF, that is, spatially confined to specific sites where the Kondo dI/dV resonance is observed in Figure 2c. We performed DFT calculations to rationalize the emergence of these magnetic moments within the Ag(111)-supported MOF (see Experimental Section). Note that this DFT approach does not address the many-body Kondo effect.[33] **Figure 4**a shows the calculated band structure of DCA_3Cu_2

on Ag(111) (without corrections for on-site Coulomb interactions between *d* electrons, that is, with Hubbard $U = 0$ for Cu and Ag). These calculations indicate a transfer of 0.20 ± 0.02 electrons per primitive unit cell from MOF to Ag(111); see Section S8, Supporting Information. Projection onto DCA_3Cu_2 MOF states (red circles in Figure 4a) shows a predominant contribution from the kagome-arranged DCA lowest unoccupied molecular orbitals (LUMOs; partially populated by Cu 4*s* electrons transferred upon metal-ligand coordination) to the near-Fermi band structure, with a very slight contribution from Cu 3*d* states[9] (see Section S13, Supporting Information, for details). Notably, the Cu 3*d* shell within the DCA_3Cu_2 kagome MOF is effectively filled, with no unpaired Cu 3*d* electrons (Section S12, Supporting Information). These calculations with $U = 0$ yielded a negligible average local magnetic moment, $\sqrt{\langle m^2 \rangle} \approx 0.05\ \mu_B$, per DCA molecule (see Experimental Section). Although the intrinsic kagome flat and Dirac bands are significantly perturbed by Ag(111) compared to the isolated MOF, the bandwidth defined by the MOF states (≈300 meV) remains similar, with remnants of the flat band[9] still observed (in particular near the Γ-point; see Figure S13, Supporting Information).

Recent theoretical work has shown electron-electron Coulomb interactions in the DCA_3Cu_2 MOF with characteristic energies of ≈3 eV, several times larger than the kagome bandwidth—even at VB electron fillings where the Fermi level is far below the flat band.[4] We, therefore, explored the effect of electron correlations by including in our DFT calculations a Hubbard *U* term accounting for corrections due to on-site Coulomb repulsion between electrons with Cu 3*d* character (see Experimental Section). Figure 4b shows the spatial distribution of magnetic moments within the DCA_3Cu_2 MOF on Ag(111) calculated for $U = 3$ eV (see Experimental Section), closely resembling that of the DCA LUMO on Ag(111)[24] and on Gr/Ir(111),[22] with some Cu contribution (due to partial hybridization between DCA LUMOs and Cu *d* orbitals). This magnetic moment density also resembles the spatial distribution of the d*I*/d*V* ZBP in Figure 2c, with significant d*I*/d*V* signal at the anthracene extremities and Cu sites (see Section S13, Supporting Information). The average magnetic moment per DCA increases monotonically as a function of *U*, reaching $\sqrt{\langle m^2 \rangle} \approx 0.28\ \mu_B$ for $U = 5$ eV (Figure 4c), similar to freestanding DCA_3Cu_2 (see Figure S17, Supporting Information). That is, interactions between MOF electrons give rise to magnetic moments residing at specific DCA kagome sites. These magnetic moments cannot be attributed to unpaired Cu 3*d* electrons since the Cu 3*d* shell within the MOF is effectively filled; they are associated with partially populated MOF VB orbitals with dominant DCA LUMO character (Section S13, Supporting Information). Agreement between experimental and simulated STM imaging (Figure 4d,e; see Experimental Section) reinforces that our DFT+*U* calculations capture the fundamental electronic properties of the Ag(111)-supported DCA_3Cu_2 kagome MOF.

We further considered a MFH model (Experimental Section) to interpret our DFT+*U* results, where the Hamiltonian of the freestanding 2D kagome crystal consists of a nearest-neighbor tight-binding (TB) term (hopping rate *t* between kagome sites) and a Hubbard interaction term, U_{MFH}, accounting for on-site Coulomb repulsion between electrons located at kagome sites (see Experimental Section; Section S9, Supporting Information). Note that this is in contrast with DFT+*U*, where *U* is a correction related to interactions between Cu 3*d* electrons (that is, $U_{MFH} \neq U$). We used $t \approx 53.5$ meV determined by fitting the non-interacting ($U_{MFH} = 0$) TB band structure (which has a bandwidth of 6*t*) to match the VB structure given by DFT (with $U = 0$) for freestanding neutrally charged DCA_3Cu_2 (Section S9, Supporting Information). For $U_{MFH} > \approx 6.5t \approx 350$ meV (and electron filling matching the charge transfer given by DFT+*U*; see Supporting Information), this model shows the emergence of magnetic moments located at kagome sites (Figure 4f; Section S9, Supporting Information), with an average magnetic moment per DCA kagome site matching closely that obtained via DFT+*U* for DCA_3Cu_2/Ag(111) for $U \geq 3$ eV (Figure 4c). Based on this MFH model, we found that partial disorder of the lattice (observed in our STM data; Figure 1) does not significantly affect these local magnetic moments (Figure S20, Supporting Information).

Our DFT+*U* and MFH calculations provide strong evidence that the magnetic moments revealed experimentally via the Kondo effect result from interactions between MOF electrons. In our calculations, the energy scale of these interactions ($U > \approx 3$ eV in DFT+*U*, $U_{MFH} > \approx 0.35$ eV in MFH model) is comparable to or larger than the kagome bandwidth, consistent with previous calculations.[4] The spatial distribution of the experimentally observed ZBPs (Figure 2c,d) is similar to that of the DFT+*U*-derived magnetic moments (Figure 4b), following the kagome-arranged DCA LUMOs and Cu atoms, consistent with the dominant LUMO and slight Cu 3*d* character of the VB (Figure 4a): on-site Coulomb repulsion between electrons *hopping* among these states give rise to local magnetic moments that become Kondo-screened by Ag(111) conduction electrons (**Figure 5**). Our calculations indicate a magnetic moment of ≈1/4 μ_B per DCA (Figure 4c); Kondo screening has been demonstrated for fractional magnetic moments of similar magnitude, experimentally[34] and theoretically.[35]

Our calculations provide a conservative lower bound estimate of the Coulomb interactions between MOF electrons, with characteristic energies that must be at least comparable to the kagome bandwidth, rationalizing the emergence of local magnetic moments, in agreement with previous studies.[4,36,37] An exact determination of the magnitude of these interactions is beyond the scope of this work and requires further investigations.

Our measurements did not reveal a direct experimental signature of an electronic flat band. This could be explained by: i) significant MOF-Ag(111) electronic hybridization (Figure 4a; Sections S7 and S8, Supporting Information); ii) above-Fermi LDOS dominated by MOF-confined, Ag(111) Shockley surface state (Figure 2a; Section S2, Supporting Information), hindering the observation of a flat-band-related LDOS feature; or iii) strong electron–electron interactions (manifested here via the Kondo effect) dramatically perturbing the MOF electronic structure and distorting the flat band.[8]

Our DFT+*U* calculations—which do not take Kondo screening into account—indicate (frustrated) antiferromagnetic coupling between MOF magnetic moments (Figure 4b), with

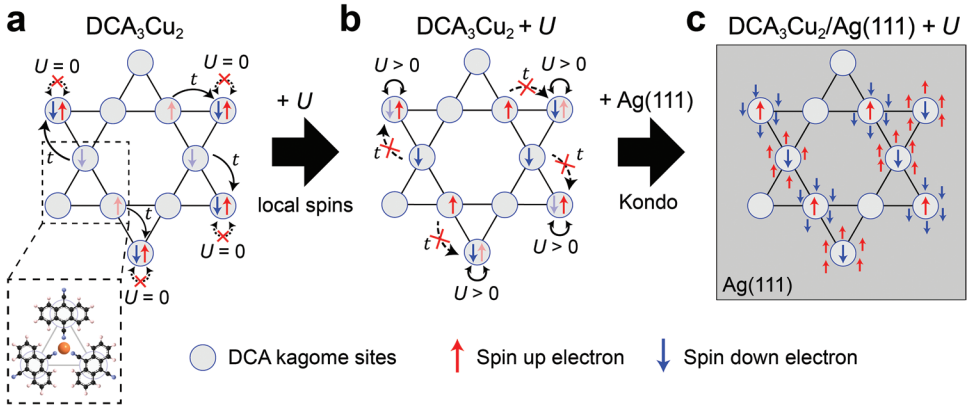

Figure 5. Electron–electron interactions, local magnetic moments, and Kondo screening in kagome DCA_3Cu_2 MOF on Ag(111). a) Schematic of 2D kagome lattice, where each circle represents a DCA site within the freestanding DCA_3Cu_2 MOF (dashed box inset: correspondence with DCA_3Cu_2 structure). Absence of on-site electron-electron Coulomb repulsion ($U = 0$) facilitates electron hopping (rate t), allowing for two electrons to occupy the same kagome site, resulting in a zero net magnetic moment ($m = 0$; arrows represent electron spin). b) Non-zero electron-electron interactions ($U > 0$) hinder inter-site electron hopping, resulting in non-zero magnetic moments ($m \neq 0$) located at kagome sites. c) On Ag(111), the spin of surface conduction electrons (represented by arrows surrounding circles) can screen the magnetic moments within the kagome MOF, resulting in a Fermi-level LDOS Kondo resonance observed via dI/dV STS.

an estimated characteristic energy <1 meV (Section S11, Supporting Information). We also estimated that the upper bound of any potential substrate-mediated Ruderman–Kittel–Kasuya–Yosida interaction energy is <10 meV. These energy scales are significantly smaller than the estimated Kondo exchange interaction (≈250 meV; Section S11, Supporting Information); in the case considered here of kagome DCA_3Cu_2 MOF on Ag(111), Kondo screening is the dominant effect and quenches any possible magnetic ordering of the kagome magnetic moments. Given these energy scales, we also rule out that the off-Fermi energy-symmetric dI/dV features in Figure 3a–c are related to inelastic spin (e.g., triplet-to-singlet) excitations.[13]

We note that our DCA_3Cu_2/Ag(111) system differs from DCA_3Cu_2 on Cu(111)[25,26] (Figures S1 and S2, Supporting Information) and other similar systems,[20,22] where the Kondo effect and strong electron-electron interactions were not observed. Based on DFT (Section S7, Supporting Information), electronic hybridization between DCA_3Cu_2 and Ag(111) seems qualitatively similar to that between DCA_3Cu_2 and Cu(111), with significant distortion of the intrinsic Dirac and flat bands. However, the MOF-to-surface electron transfer is significantly larger on Cu(111) (≈0.7e^- per primitive unit cell) than on Ag(111) (≈0.2e^-). This indicates a stronger interaction on Cu(111) than on Ag(111), consistent with the difference in chemical reactivity of both surfaces[38] and previous studies of DCA/Ag(111)[24] and DCA/Cu(111).[25] Importantly, it suggests a reduced effect of electron–electron interactions on Cu(111) due to a smaller kagome VB population. The balanced interactions with Ag(111) allow the MOF to retain its fundamental electronic properties, with the Fermi level close to the MOF Dirac point (resulting in significant electron–electron interactions), and with Ag(111) providing a reservoir of conduction electrons that enables the measurement of the Kondo effect. The latter serves as a direct experimental probe of magnetic moments which, as unambiguously shown by our DFT+U and MFH calculations, emerge from strong electron correlations within the 2D kagome MOF.

3. Conclusion

Our study provides compelling evidence of locally confined magnetic moments in a 2D kagome MOF, revealed experimentally via the measurement of the Kondo effect. These magnetic moments result from strong electron-electron Coulomb interactions within the MOF; these interactions are the direct consequence of the intrinsic kagome geometry of the MOF. Here, we used the Kondo effect—a well-studied and well-understood many-body phenomenon—as a probe for electronic correlations within the 2D MOF. Our findings are similar to the recently discovered correlated electron phases in 2D material twisted layers hosting flat bands,[39] with the benefit that, here, the electronic structure and resulting electron correlations are dictated by the intrinsic geometry of the molecular self-assembly and metal-ligand coordination, without the need of a precisely controlled twist angle. We envision that 2D organic materials, with morphologies (e.g., kagome) that give rise to strong electronic correlations, and interfaced with wide bandgap materials (e.g., 2D semiconductors or insulators) where their intrinsic electronic and magnetic properties are retained, will open the door to solid-state technologies where a wide range of quantum correlated electron (e.g., metal-to-insulator transitions), magnetic and topologically nontrivial phases can be achieved by control of the Fermi level (e.g., electrostatic gating).

4. Experimental Section

Sample Preparation: The atomically thin DCA_3Cu_2 kagome MOF on Ag(111) was synthesized in ultrahigh vacuum (UHV) by depositing DCA molecules (Tokyo Chemical Industry; > 95% purity) and Cu atoms (>99.99% purity) from the gas phase onto a clean Ag(111) surface (obtained by repeated cycles of Ar^+ sputtering and annealing at 790 K). Two different sample preparation procedures were considered: i) co-deposition of DCA and Cu onto Ag(111) held at room temperature; ii) sequential deposition of DCA followed by Cu onto Ag(111) held at ≈100 K. Procedure (i) yielded <10% MOF coverage, with high coverage

of DCA-only domains. Procedure (ii) yielded >60% MOF coverage. Subsequent annealing at RT led to significantly less MOF coverage and an increased amount of Cu clusters and DCA-only domains, indicating that the kagome DCA_3Cu_2 structure on Ag(111) was metastable, as previously suggested.[40] Base pressure during molecular and metal depositions was $<5 \times 10^{-10}$ mbar.

STM & dI/dV STS Measurements: All STM and d*I*/d*V* STS measurements were performed at 4.4 K in UHV ($<1\times10^{-10}$ mbar) with an Ag-terminated Pt/Ir tip, unless otherwise stated. Topographic STM images were acquired in constant-current mode with sample bias reported throughout the text. All d*I*/d*V* STS measurements, unless otherwise stated, were performed by recording the tunneling current as a function of tip-sample bias voltage in the junction, with tip-sample distance stabilized with respect to a specified tunneling current and bias voltage set point at a fixed reference location. The *I*–*V* data were then numerically differentiated to obtain *dI/dV* as a function of bias voltage. All d*I*/*dV* maps were obtained with a lock-in technique by applying a small modulation of 10 mV (peak amplitude) at 1.13 kHz frequency to the bias voltage. The d*I*/d*V* maps in Figure 2 were acquired using a multi-pass (MP) approach. This technique consists of: i) acquiring a constant-current STM topographic profile along a scanning line (set point $V_b = -200$ mV, $I_t = 500$ pA, scanning speed 1.6 nm s^{-1}); ii) recording d*I*/d*V* with lock-in amplifier (10 mV bias voltage modulation, 1.13 kHz; see above) while scanning (speed: 0.8 nm s^{-1}) the same line and following the same constant-current STM topographic profile as in (i) but with the tip retracted 120 pm and 30 pm for Figure 2c and 2d, respectively; and iii) repeating this procedure sequentially for each scanned line of the map. This approach has the benefit of minimizing variations of d*I*/d*V* due to changes in STM apparent topography. The STM image in Figure 4e was obtained using a tip functionalized with a carbon monoxide (CO) molecule (see below).

Nc-AFM Measurements: All nc-AFM measurements were performed at 4.4 K in UHV ($<1\times10^{-10}$ mbar) with a qPlus sensor (resonance frequency, $f_0 \approx 30$ kHz, spring constant, $K \approx 1.8$ kN m^{-1}, amplitude modulation: 60 pm) with an Ag-terminated Pt/Ir tip. Unless otherwise stated, the tip was functionalized with a CO molecule[41] by introducing CO gas into the UHV chamber (5×10^{-8} mbar for ≈3 s) with the sample at 4.4 K and picking up a CO molecule on bare Ag(111) (or bare Cu(111); see Supporting Information) with the tip. Nc-AFM imaging was performed at a constant tip height stabilized with respect to a specified tunneling current and bias voltage set point at a fixed reference location.

Temperature-Dependent dI/dV STS: The base temperature of the system was kept at 4.4 K for d*I*/d*V* STS measurements performed for temperatures up to ≈70 K. The STM was heated to a specified temperature (by applying power to built-in Zener diode) and was stabilized at that temperature for 1–1.5 h to allow thermal drift to settle prior to data acquisition. At higher temperatures, a drift correction software was employed to compensate for any residual thermal drift. For STS measurements performed above 77 K, the STM was heated from a base temperature of 77 K. For all temperature-dependent d*I*/d*V* STS data, the same STM set point of $V_b = -250$ mV, $I_t = 1.5$ nA was used. Effects of thermal broadening were included in the fitting of d*I*/d*V* spectra[28] (see main text and Section S6, Supporting Information).

DFT Calculations: DFT calculations were performed as implemented in the Vienna Ab-initio Simulation Package (VASP),[42] with the Perdew–Burke–Ernzerhof functional under the generalized gradient approximation to describe exchange-correlation effects[43] and projector augmented wave pseudopotentials.[44,45] A 400 eV cut-off was used for the plane wave basis set. A semi-empirical potential developed by Grimme (DFT-D3) was used to describe van der Waals forces.[46] For an enhanced description of correlations between *d* electrons, Dudarev's implementation[47] of DFT+*U* was used. A systematic variation of *U* was considered (see Figure 4c; with $U \geq 3$V consistent with literature[48]); *U* represents a correction energy term accounting for interactions between *Cu* 3*d* electrons ($U = 0$ was used for the substrate unless otherwise indicated; see Supporting Information).

Structural relaxations were performed with a $3 \times 3 \times 1$ Monkhorst-Pack Γ-centered *k*-points grid, with ionic positions relaxed until the Hellman-Feynman force on each atom was <0.01 eV/Å. Relaxation of freestanding DCA_3Cu_2 (DCA_3Cu_2 on metal substrate) used Gaussian smearing with a width of 0.05 eV (first order Methfessel Paxton smearing with a width of 0.2 eV, respectively).

For calculations on a metal substrate, a three-atom-thick metal slab was used for the substrate, with hydrogen atoms on the bottom surface as a passivation layer. Only the two top layers were structurally relaxed; the bottom layer of metal atoms was kept fixed at their bulk coordinates. 15 Å of vacuum spacing was included above the slab to minimize possible interactions with its image resulting from periodic boundary conditions. For comparison, calculations with a four-atom-thick metal slab as the substrate were also performed , resulting in fundamentally identical charge density, MOF-to-surface electron transfer, and magnetic moments as for the three-atom-thick case.

For DCA_3Cu_2 kagome on Ag(111), a supercell of 7×7 Ag surface atoms was used, with the experimental bulk lattice constant[49] of 2.889 Å, and with the MOF commensurate with the underlying substrate (periodic boundary conditions required by computation; see Figure 4b). For DCA_3Cu_2 kagome on Cu(111), a supercell of 8×8 Cu surface atoms was used, with the experimental bulk lattice constant[49] of 2.554 Å, and a MOF adsorption geometry given by the nc-AFM measurements (Figure S2b, Supporting Information).

The electronic structure of DCA_3Cu_2 was calculated (in the freestanding case, on Ag(111), and on Cu(111); without spin polarization) using a grid of $7 \times 7 \times 1$ *k*-points, self-consistently until the energy changed by less than 10^{-4} eV between steps. Tetrahedral interpolation with Blöchl corrections was used for Brillouin zone integration. These parameters allowed for convergence of charge density. For calculations with spin polarization, an $11 \times 11 \times 1$ *k*-point grid and an energy convergence criterion of $<1 \times 10^{-6}$ eV were used due to small energy scales involved for different spin configurations. The DOS was calculated with a $15 \times 15 \times 1$ *k*-point grid and Gaussian smearing with a width of 0.05 eV while keeping the charge density constant. Dipole corrections to the electrostatic potential perpendicular to the slab were included in the electronic structure calculations.

For calculations of spin density of the DCA_3Cu_2 MOF (e.g., Figure 4b), initial conditions were considered where each DCA molecule, in a single unit cell, was either positively spin-polarized (1), negatively spin-polarized (–1), or had zero spin polarization (0). This was achieved by setting the magnetic moment for each carbon atom in a single DCA molecule to $+1\ \mu_B$, $-1\ \mu_B$, or $0\ \mu_B$, respectively. The authors trialed each unique combination of initial DCA spin polarization configuration in a single unit cell up to symmetry (i.e., (0, 0, 0), (1, 0, 0), (1, –1, 0), (1, 1, 0), (1, 1, –1), (1, 1, 1); 3 DCA molecules in a single unit cell). The lowest energy magnetic configuration was recorded after calculating to self-consistency.

Charge and magnetic moments were calculated by partitioning using DDEC6 in order to assign spin and charge to the components of the DCA_3Cu_2 kagome MOF and the metal substrate.[50–53] Partitioning with Bader charge analysis was also performed for comparison.[54] It was found that the electron transferred from MOF to metal surface (0.20 ± 0.02 electrons per primitive unit for DCA_3Cu_2/Ag(111); Section S8, Supporting Information), calculated by DDEC was more robust than that calculated by Bader. The calculated electron transfer varied, however, slightly as a function of *U* and was reflected in the uncertainty of the electron transfer. Spin analysis was consistent between Bader and DDEC. The magnetic moment on each DCA molecule was calculated as the sum of magnetic moments on the atoms of that DCA molecule. The average local magnetic moment, $\sqrt{\langle m^2 \rangle}$, was the root-mean-square of all the DCA magnetic moments in a single unit cell.

For isolated molecules, such as DCA (or Cu_2DCA in Supporting Information), calculations were performed by only considering the Γ point, with a Gaussian smearing width of 0.05 eV and no van der Waals corrections. Vibrational modes (see Supporting Information) were calculated via the Hessian matrix and central differences with a step size of 0.015 Å, as implemented in VASP.

All structure visualization was performed with the VESTA software package.[55] PyProcar was used for post-processing of projected band structures.[56]

MFH Model: To gain insight into how electron-electron interactions, unit cell size (e.g., primitive or supercell), electron filling, and disorder affect the electronic and magnetic properties of the kagome MOF, a Hubbard model was used, solved via the Hartree-Fock mean-field approximation assuming collinear spins (equivalent to Hartree theory). This approximation assumes a single-electron problem with a potential depending on electron density, determined self-consistently from the single-electron eigenstates.[57] The MFH model treats many-body effects similarly to DFT, albeit with a simpler potential. The MFH Hamiltonian is:

$$H = -t\sum_{\langle i,j\rangle,\sigma}\left(c^{\dagger}_{i,\sigma}c_{j,\sigma}\right) + U_{\mathrm{MFH}}\sum_{i}\left(n_{i,\uparrow}\left\langle n_{i,\downarrow}\right\rangle + n_{i,\downarrow}\left\langle n_{i,\uparrow}\right\rangle - \left\langle n_{i,\uparrow}\right\rangle\left\langle n_{i,\downarrow}\right\rangle\right) \tag{4}$$

where $c^{\dagger}_{i,\sigma}$ creates a spin σ at lattice site i, $n_{i,\sigma}$ is the number operator for spin σ electrons at site i, and $\langle n_{i,\sigma}\rangle$ is the average or "mean-field" spin σ electron density at site i (taking values between 0 and 1). The parameter t is the nearest-neighbor hopping parameter; its corresponding sum was taken over nearest-neighbor pairs. Parameter U_{MFH} is the Hubbard on-site Coulomb interaction energy parameter, which was related but distinct from the correction U in DFT+U. Here, U_{MFH} represents all electron-electron interactions, on the basis of the kagome lattice, while the U in DFT+U accounts for interactions between Cu 3*d* electrons, not captured accurately by the Hartree and approximate exchange-correlation functionals.

The MFH Hamiltonian was solved numerically with an algorithm written in Python that is summarized in the following. A random electron density $\langle n_{i,\sigma}\rangle$ was used as an initial ansatz, produced by a symmetric Dirichlet distribution with a high concentration parameter for the spin up and down electron densities separately. Keeping the mean-field electron density constant, the MFH Hamiltonian was divided into spin up and down terms, and solved for its single particle eigenvalues $\varepsilon_{j,\sigma}$ and eigenvectors $v_{i,j,\sigma}$ (with i indexing site, j indexing eigenstate and σ indexing spin). The new electron density was determined by filling eigenstates according to the Fermi Dirac distribution:

$$f_{\mathrm{FD}}(E,T) = 1/\left(e^{E/T}+1\right) \tag{5}$$

using a small "temperature" T (T = 0.1t was used). The chemical potential μ was found by solving for the total electron number N_e:

$$N_e = \sum_{j,\sigma} f_{\mathrm{FD}}\left(\varepsilon_{j,\sigma}-\mu,T\right) \tag{6}$$

The output electron density was obtained from the eigenvectors by:

$$\left\langle n^{\mathrm{out}}_{i,\sigma}\right\rangle = \sum_{j} f_{\mathrm{FD}}\left(\varepsilon_{j,\sigma}-\mu,T\right)\left|v_{i,j,\sigma}\right|^2 \tag{7}$$

and the total energy by:

$$E = \sum_{j,\sigma} f_{\mathrm{FD}}\left(\varepsilon_{j,\sigma}-\mu,T\right)\varepsilon_{j,\sigma} - U_{\mathrm{MFH}}\sum_{i}\left\langle n_{i,\uparrow}\right\rangle\left\langle n_{i,\downarrow}\right\rangle \tag{8}$$

The difference between the input and output electron densities was quantified by the residual:

$$\sqrt{\sum_{i}\left(\left\langle n^{\mathrm{out}}_{i,\sigma}\right\rangle - \left\langle n^{\mathrm{in}}_{i,\sigma}\right\rangle\right)^2} \tag{9}$$

If the residual was sufficiently small, then the calculation reached self-consistency. Otherwise, a new electron density ansatz was constructed by either simple mixing of new and old electron densities or direct inversion of the iterative subspace (DIIS; also known as Pulay mixing[58]), and the process was repeated. Simple mixing sets the new density to be a linear combination of the input and output densities:

$$\left\langle n_{i,\sigma}\right\rangle = \alpha\left\langle n^{\mathrm{out}}_{i,\sigma}\right\rangle + (1-\alpha)\left\langle n^{\mathrm{in}}_{i,\sigma}\right\rangle \tag{10}$$

where α is an empirically chosen parameter between 0 and 1. Once simple mixing reduced the residual <0.01, the authors changed to using DIIS[58] using the algorithm of Ref. [59], until the residual was $<10^{-4}$.

For MFH calculations of magnetic moments in the kagome lattice (Figure 4f), a 6×6 supercell was used with periodic boundary conditions and a 4×4 Monkhorst-Pack k-point grid. Energy units of t were taken. To search for the ground state, different initial electron densities were sampled, stepping through ratios of spin up to spin down electrons, and trialing several different random initial configurations for each initial magnetization. A fully non-magnetic configuration was also trialed. Among these trials, the one with the lowest energy after converging to self-consistency was kept and its data reported.

For a direct comparison with the DFT results, calculations were also performed with a primitive unit cell (3 kagome sites) with periodic boundary conditions while sampling the Brillouin zone with a 25×25 Monkhorst-Pack k-point grid. The DFT spin configuration on the DCA molecules was fit to the results of the MFH model to find the Hubbard U_{MFH} which minimized the difference between DFT and MFH spin densities (as measured by the root-mean-square difference). The DFT spin density and a uniform charge density were used as the initial configuration for the MFH model in this fitting calculation. Note that the greater configurational freedom for the supercell compared to the primitive unit cell results in an enhanced average local magnetic moment (Figure 4c) and a richer magnetic configuration (Figure 4f; Section S9, Supporting Information).

The parameters of interest were the magnetic moments on each kagome site i:

$$m^{(i)} = \left\langle n_{i,\uparrow}\right\rangle - \left\langle n_{i,\downarrow}\right\rangle \tag{11}$$

the net magnetization:

$$\langle m\rangle = \sum_{i}\left(\left\langle n_{i,\uparrow}\right\rangle - \left\langle n_{i,\downarrow}\right\rangle\right)/N_{\mathrm{sites}} \tag{12}$$

where N_{sites} is the number of sites in the lattice, and the average magnitude of the local magnetic moment on each kagome lattice site:

$$\sqrt{\langle m^2\rangle} = \sqrt{\left(\sum_{i}\left(\left\langle n_{i,\uparrow}\right\rangle - \left\langle n_{i,\downarrow}\right\rangle\right)^2\right)}/N_{\mathrm{sites}} \tag{13}$$

STM Imaging Simulation: The simulated STM image in Figure 4d was derived from DFT+U calculations using the Tersoff-Hamann approximation as implemented in HIVE-STM,[60] integrating over states from –100 meV to the Fermi level.

Supporting Information

Supporting Information is available from the Wiley Online Library or from the author.

Acknowledgements

D.K., Y.Y., and N.V.M. acknowledge funding support from the Australian Research Council (ARC) Centre of Excellence in Future Low-Energy Electronics Technologies (CE170100039). A.S. acknowledges funding support from the ARC Future Fellowship scheme (FT150100426). B.F. and N.M. gratefully acknowledge the computational support from National Computing Infrastructure and Pawsey Supercomputing Facility. B. F. and B.L. are supported through Australian Government Research Training Program (RTP) Scholarships. The authors also thank Ben Powell for his helpful advice regarding the mean-field Hubbard method.

Conflict of Interest

The authors declare no conflict of interest.

Data Availability Statement

The data that support the findings of this study are available from the corresponding author upon reasonable request.

Keywords

2D organic nanomaterials, correlated electron materials, kondo effect, metal–organic frameworks, non-contact atomic force microscopy, on-surface self-assembly, scanning tunneling microscopy

Received: August 2, 2021
Revised: August 27, 2021
Published online: September 12, 2021

[1] S. Sachdev, *Phys. Rev. B* **1992**, *45*, 12377.
[2] L. Zheng, L. Feng, W. Yong-Shi, *Chinese Phys. B* **2014**, *23*, 77308.
[3] A. Alexandradinata, N. P. Armitage, A. Baydin, W. Bi, Y. Cao, H. J. Changlani, E. Chertkov, E. H. Neto, L. Delacretaz, I. El Baggari, arXiv:2010.00584, v1, **2020**.
[4] M. Fuchs, P. Liu, T. Schwemmer, G. Sangiovanni, R. Thomale, C. Franchini, D. Di Sante, *J. Phys.: Mater.* **2020**, *3*, 025001.
[5] Z. Lin, J. H. Choi, Q. Zhang, W. Qin, S. Yi, P. Wang, L. Li, Y. Wang, H. Zhang, Z. Sun, L. Wei, S. Zhang, T. Guo, Q. Lu, J. H. Cho, C. Zeng, Z. Zhang, *Phys. Rev. Lett.* **2018**, *121*, 96401.
[6] S. S. Zhang, J.-X. Yin, M. Ikhlas, H.-J. Tien, R. Wang, N. Shumiya, G. Chang, S. S. Tsirkin, Y. Shi, C. Yi, *Phys. Rev. Lett.* **2020**, *125*, 46401.
[7] C. Broholm, R. J. Cava, S. A. Kivelson, D. G. Nocera, M. R. Norman, T. Senthil, *Science* **2020**, *367*, eaay0668.
[8] T. Ohashi, N. Kawakami, H. Tsunetsugu, *Phys. Rev. Lett.* **2006**, *97*, 66401.
[9] L. Z. Zhang, Z. F. Wang, B. Huang, B. Cui, Z. Wang, S. X. Du, H.-J. Gao, F. Liu, *Nano Lett.* **2016**, *16*, 2072.
[10] G. Chen, A. L. Sharpe, E. J. Fox, Y.-H. Zhang, S. Wang, L. Jiang, B. Lyu, H. Li, K. Watanabe, T. Taniguchi, *Nature* **2020**, *579*, 56.
[11] Y. Choi, H. Kim, Y. Peng, A. Thomson, C. Lewandowski, R. Polski, Y. Zhang, H. S. Arora, K. Watanabe, T. Taniguchi, *Nature* **2021**, *589*, 536.
[12] M. Ternes, A. J. Heinrich, W. D. Schneider, *J. Phys.: Condens. Matter* **2009**, *21*, 053001.
[13] A. Mugarza, C. Krull, R. Robles, S. Stepanow, G. Ceballos, P. Gambardella, *Nat. Commun.* **2011**, *2*, 490.
[14] L. Ye, M. Kang, J. Liu, F. Von Cube, C. R. Wicker, T. Suzuki, C. Jozwiak, A. Bostwick, E. Rotenberg, D. C. Bell, *Nature* **2018**, *555*, 638.
[15] J.-X. Yin, W. Ma, T. A. Cochran, X. Xu, S. S. Zhang, H.-J. Tien, N. Shumiya, G. Cheng, K. Jiang, B. Lian, *Nature* **2020**, *583*, 533.
[16] B. Cui, X. Zheng, J. Wang, D. Liu, S. Xie, B. Huang, *Nat. Commun.* **2020**, *11*, 66.
[17] L. Dong, Z. A. Gao, N. Lin, *Prog. Surf. Sci.* **2016**, *91*, 101.
[18] D. Cui, D. F. Perepichka, J. M. MacLeod, F. Rosei, *Chem. Soc. Rev.* **2020**, *49*, 2020.
[19] G. Galeotti, F. De Marchi, E. Hamzehpoor, O. MacLean, M. Rajeswara Rao, Y. Chen, L. V. Besteiro, D. Dettmann, L. Ferrari, F. Frezza, P. M. Sheverdyaeva, R. Liu, A. K. Kundu, P. Moras, M. Ebrahimi, M. C. Gallagher, F. Rosei, D. F. Perepichka, G. Contini, *Nat. Mater.* **2020**, *19*, 874.
[20] L. Yan, O. J. Silveira, B. Alldritt, O. Krejčí, A. S. Foster, P. Liljeroth, *Adv. Funct. Mater.* **2021**, *31*, 2100519.
[21] C.-H. Hsu, J. Liu, F.-C. Chuang, R. Zhang, B. Xia, H. Xu, L. Huang, Q. Jin, P. N. Liu, N. Lin, *Nanoscale* **2019**, *11*, 878.
[22] A. Kumar, K. Banerjee, A. S. Foster, P. Liljeroth, *Nano Lett.* **2018**, *18*, 5596.
[23] L. Yan, I. Pohjavirta, B. Alldritt, P. Liljeroth, *ChemPhysChem* **2019**, *20*, 2297.
[24] D. Kumar, C. Krull, Y. Yin, N. V. Medhekar, A. Schiffrin, *ACS Nano* **2019**, *13*, 11882.
[25] J. Zhang, A. Shchyrba, S. Nowakowska, E. Meyer, T. a Jung, M. Muntwiler, *Chem. Commun.* **2014**, *50*, 12289.
[26] L. Hernández-López, I. Piquero-Zulaica, C. A. Downing, M. Piantek, J. Fuji, D. Serrate, E. Ortega, F. Bartolomé, J. Lobo-Checa, *Nanoscale* **2021**, *13*, 5216.
[27] Y. Pennec, W. Auwärter, A. Schiffrin, A. Weber-Bargioni, A. Riemann, J. V. Barth, *Nat. Nanotechnol.* **2007**, *2*, 99.
[28] K. Nagaoka, T. Jamneala, M. Grobis, M. F. Crommie, *Phys. Rev. Lett.* **2002**, *88*, 077205.
[29] A. Zhao, Q. Li, L. Chen, H. Xiang, W. Wang, S. Pan, B. Wang, X. Xiao, J. Yang, J. G. Hou, Q. Zhu, *Science* **2005**, *309*, 1542.
[30] F. Bischoff, Y. He, K. Seufert, D. Stassen, D. Bonifazi, J. V. Barth, W. Auwärter, *Chem. - Eur. J.* **2016**, *22*, 15298.
[31] B. C. Stipe, M. A. Rezaei, W. Ho, *Science* **1998**, *280*, 1732.
[32] I. Fernández-Torrente, K. J. Franke, J. I. Pascual, *Phys. Rev. Lett.* **2008**, *101*, 217203.
[33] P. P. Baruselli, M. Fabrizio, A. Smogunov, R. Requist, E. Tosatti, *Phys. Rev. B* **2013**, *88*, 245426.
[34] M. Garnica, D. Stradi, S. Barja, F. Calleja, C. Díaz, M. Alcamí, N. Martín, A. L. Vázquez de Parga, F. Martín, R. Miranda, *Nat. Phys.* **2013**, *9*, 368.
[35] A. Agarwala, V. B. Shenoy, *Phys. Rev. B* **2016**, *93*, 241111.
[36] Z. Wang, P. Jain, K.-Y. Choi, J. Van Tol, A. K. Cheetham, H. W. Kroto, H.-J. Koo, H. Zhou, J. Hwang, E. S. Choi, *Phys. Rev. B* **2013**, *87*, 224406.
[37] E. Cockayne, E. B. Nelson, *J. Chem. Phys.* **2015**, *143*, 024701.
[38] J. V. Barth, J. Weckesser, N. Lin, A. Dmitriev, K. Kern, *Appl. Phys. A* **2003**, *76*, 645.
[39] Y. Cao, V. Fatemi, A. Demir, S. Fang, S. L. Tomarken, J. Y. Luo, J. D. Sanchez-Yamagishi, K. Watanabe, T. Taniguchi, E. Kaxiras, *Nature* **2018**, *556*, 80.
[40] S. Krotzky, C. Morchutt, V. S. Vyas, B. V. Lotsch, R. Gutzler, K. Kern, *J. Phys. Chem. C* **2016**, *120*, 4403.
[41] J. Repp, G. Meyer, S. M. Stojković, A. Gourdon, C. Joachim, *Phys. Rev. Lett.* **2005**, *94*, 26803.
[42] G. Kresse, J. Furthmüller, *Comput. Mater. Sci.* **1996**, *6*, 15.
[43] J. P. Perdew, K. Burke, M. Ernzerhof, *Phys. Rev. Lett.* **1996**, *77*, 3865.
[44] P. E. Blöchl, *Phys. Rev. B* **1994**, *50*, 17953.
[45] D. Joubert, *Phys. Rev. B* **1999**, *59*, 1758.
[46] S. Grimme, J. Antony, S. Ehrlich, H. Krieg, *J. Chem. Phys.* **2010**, *132*, 154104.
[47] S. Dudarev, G. Botton, *Phys. Rev. B* **1998**, *57*, 1505.
[48] S. A. Tolba, K. M. Gameel, B. A. Ali, H. A. Almossalami, N. K. Allam, in *Density Functional Calculations: Recent Progresses Theory Applications* (Ed.: G. Yang), IntechOpen, London **2018**, Ch. 1.
[49] R. R. John, *CRC Handbook of Chemistry and Physics*, CRC Press, Boca Raton, FL **2019**.
[50] T. A. Manz, D. S. Sholl, *J. Chem. Theory Comput.* **2011**, *7*, 4146.
[51] T. A. Manz, N. G. Limas, *RSC Adv.* **2016**, *6*, 47771.
[52] N. G. Limas, T. A. Manz, *RSC Adv.* **2016**, *6*, 45727.
[53] T. A. Manz, N. G. Limas, *Program Computing DDEC Atomic Charges*, ddec.sourceforge.net (accessed: October 2020).
[54] W. Tang, E. Sanville, G. Henkelman, *J. Phys.: Condens. Matter* **2009**, *21*, 084204.
[55] K. Momma, F. Izumi, *J. Appl. Crystallogr.* **2011**, *44*, 1272.
[56] U. Herath, P. Tavadze, X. He, E. Bousquet, S. Singh, F. Munoz, A. H. Romero, *Comput. Phys. Commun.* **2020**, *251*, 107080.
[57] J. R. Reimers, *Computational Methods for Large Systems: Electronic Structure Approaches for Biotechnology and Nanotechnology*, John Wiley & Sons, Hoboken, NJ **2011**.
[58] P. Pulay, *Chem. Phys. Lett.* **1980**, *73*, 393.
[59] T. Rohwedder, R. Schneider, *J. Math. Chem.* **2011**, *49*, 1889.
[60] D. E. P. Vanpoucke, G. Brocks, *Phys. Rev. B* **2008**, *77*, 241308.